Biomicrofluidics ARTICLE scitation.org/journal/bmf

Experimental and numerical study of elasto-inertial focusing in straight channels

Cite as: Biomicrofluidics 13, 034103 (2019); doi: 10.1063/1.5093345
Submitted: 20 February 2019 · Accepted: 22 April 2019 ·
Published Online: 9 May 2019

Mohammad Amin Raoufi,[1,2,3,a)] Ali Mashhadian,[4,a)] Hamid Niazmand,[3] Mohsen Asadnia,[2] Amir Razmjou,[5] and Majid Ebrahimi Warkiani[1,6,b)]

AFFILIATIONS

[1]School of Biomedical Engineering, University of Technology Sydney, Sydney 2007, NSW, Australia
[2]School of Engineering, Macquarie University, Sydney 2109, NSW, Australia
[3]Department of Mechanical Engineering, Ferdowsi University of Mashhad, Mashhad, Iran
[4]Department of Mechanical Engineering, Sharif University, Tehran, Iran
[5]UNESCO Center for Membrane Science and Technology, School of Chemical Science and Engineering, University of New South Wales, Sydney 2052, NSW, Australia
[6]Institute of Molecular Medicine, Sechenov First Moscow State University, Moscow 119991, Russia

[a)]**Contributions:** M. A. Raoufi and A. Mashhadian contributed equally to this work.
[b)]**Author to whom correspondence should be addressed:** majid.warkiani@uts.edu.au

ABSTRACT

Elasto-inertial microfluidics has drawn significant attention in recent years due to its enhanced capabilities compared to pure inertial systems in control of small microparticles. Previous investigations have focused mainly on the applications of elasto-inertial sorting, rather than studying its fundamentals. This is because of the complexity of simulation and analysis, due to the presence of viscoelastic force. There have been some investigative efforts on the mechanisms of elasto-inertial focusing in straight channels; however, these studies were limited to simple rectangular channels and neglected the effects of geometry and flow rates on focusing positions. Herein, for the first time, we experimentally and numerically explore the effects of elasticity accompanying channel cross-sectional geometry and sample flow rates on the focusing phenomenon in elasto-inertial systems. The results reveal that increasing the aspect ratio weakens the elastic force more than inertial force, causing a transition from one focusing position to two. In addition, they show that increasing the angle of a channel corner causes the elastic force to push the particles more efficiently toward the center over a larger area of the channel cross section. Following on from this, we proposed a new complex straight channel which demonstrates a tighter focusing band compared to other channel geometries. Finally, we focused *Saccharomyces cerevisiae* cells (3–5 μm) in the complex channel to showcase its capability in focusing small-size particles. We believe that this research work improves the understanding of focusing mechanisms in viscoelastic solutions and provides useful insights into the design of elasto-inertial microfluidic devices.

I. INTRODUCTION

Microfluidics deals with the manipulation and precise control of flows geometrically restricted to sub-millimeter scales. Microfluidic devices can be categorized as either passive or active, depending on the source of the manipulating forces.[1] While majority of microfluidic devices work in a Stokes flow regime and at low-Reynolds number ($Re = \rho_f U_{max} D_H/\mu$, where ρ_f is the fluid density, U_{max} is the maximum flow velocity, D_H is the hydraulic diameter, and μ is the fluid dynamic viscosity),[2–5] inertial microfluidic devices work within intermediate *Re* numbers between Stokes and turbulent regimes.[6,7] The lateral migration of flowing particles inside a tube was first discovered by Segre and Silberberg about 60 years ago.[8] However, inertial microfluidics was first demonstrated by Di Carlo *et al.*[9] in 2007, and since then, it has been widely used for a variety of applications, including cell isolation,[10–13] blood fractionation,[14,15] cell separation,[16,17] cytometry,[18,19] and filtration.[20–22]

Conventional inertial microfluidic devices have been working with Newtonian solutions flowing through patterned nonstructured

channels such as spiral, serpentine, and expansion-contraction with rectangular, square, and trapezoidal cross sections.[12,23,24] While these devices have been capable of sorting bioparticles for various biomedical applications, their usage has been limited to particles larger than 6 μm [i.e., larger than a red blood cell (RBC)] due to the strong correlation between particle size and inertial lift forces.[25] To passively control smaller microparticles in Newtonian solutions, either the channel length has to be increased, making the device footprint impractical, or the channel hydraulic diameter needs to be reduced,[26,27] which increases the pressure drop to an extent that the whole device becomes impractical.

To address this problem, investigators have recently started to use viscoelastic solutions such as polyvinylpyrrolidone (PVP), polyacrylamide (PAA), and polyethylene oxide (PEO). For example, Faridi *et al.*[28] used sheath viscoelastic flow to separate 5 and 2 μm particles, as the 5 μm particles focus at the center while the 2 μm particles remain scattered in the pinched flow near the channel walls. In another study, using expansion-contraction cavities, Yuan *et al.*[29] focused 3.2 and 4.8 μm particles in 500 ppm PEO solution. In viscoelastic fluids, due to the extra viscoelastic forces arising from the gradients of normal stresses [$N_1(\dot{\gamma}) = \sigma_{XX} - \sigma_{YY}$, $N_2(\dot{\gamma}) = \sigma_{YY} - \sigma_{ZZ}$], particle focusing can happen even in very low *Re* numbers.[30,31] It has been proven that fluid elasticity directs flowing particles toward the lowest shear gradient regions, which are the centerline and corners for a rectangular Poiseuille flow[32] and the centerline for cylindrical Poiseuille flow.[33] So far, several research studies have been performed on the applications of elasto-inertial microfluidics including cell stretching measurements,[34] size-based cell separation,[35,36] sheath flow particle separation,[37] sheathless particle focusing,[38,39] and Dean-flow-coupled elasto-inertial particle focusing,[29,40] with particle sizes ranging from tens of micrometers down to nanoscale. However, only a limited number of studies have focused on the fundamentals and mechanisms of elasto-inertial focusing. For example, in 2016, Xiang *et al.*[31] studied elasto-inertial focusing in curved channels both numerically and experimentally. Their results revealed that the contribution of Dean forces in focusing is only important at high flow rates causing the particles to focus near the outer edge of the channel. Yang *et al.*[39] experimentally investigated the effects of elasticity on particle focusing in a straight rectangular channel and observed that even a low level of elasticity can cause particles to focus at the channel center. Li *et al.*[41] carried out a numerical study of the lateral migration of spherical particles through a square channel. They showed that secondary flows around particles and shear-thinning effects tend to push the particle toward the channel wall. Patankar *et al.*[42] investigated the effect of viscoelasticity on lateral migration of a single particle by the direct numerical simulation (DNS) method. They showed that in an Oldroyd-B fluid, elastic shear stress has an insignificance effect on the lift force, and the major impact of viscoelasticity is on the pressure. Seo *et al.*[33] studied the effect of flow rate, blockage ratio, and the shear-thinning properties of PEO and PVP solutions on the focusing of 15 μm particles in a straight channel. Their results showed that while under a pure viscoelastic condition, particles focus at the center and the corners of the channel, under the combined effect of inertia and elasticity, the particles focus at the center of the channel. The channel geometry used in these studies was rectangular, for ease of fabrication and simulation. While informative, none of these prior research studies has experimentally and numerically examined the effects of channel geometry, solution viscoelasticity, and sample flow rate on the focusing behavior of elasto-inertial systems.

In this paper, we commenced with experimental investigation of the focusing patterns of 10 and 5 μm particles in square, rectangular, and trapezoidal straight channels using a viscoelastic solution (PEO). Then, by modeling particle fluid interactions using a direct numerical simulation (DNS) method, for the first time, we studied the effect of channel geometry and corner angle on particle focusing in viscoelastic solutions. Based on that work, we proposed a novel complex straight channel in order to achieve tighter focusing compared to other channels under the same conditions. The complex channel was first numerically modeled and then tested with 5 and 3 μm particles for validation and comparison with other channels. Finally, as a proof of concept, we showcased focusing of *Saccharomyces cerevisiae* cells (3–5 μm size) through the complex channel to prove its suitability for focusing of biological samples.

II. NUMERICAL SIMULATION

A. Background

The lateral movement of neutrally buoyant particles in a shear-thinning viscoelastic solution flowing through a microchannel mainly originates from four different lift forces, including shear gradient (F_S), wall induced (F_W), Magnus (F_Ω), and elastic (F_E) forces. Generally, inertial forces can be considered negligible unless the particle size becomes comparable to the characteristic length of the channel, $a/D_H > 0.07$, where a and D_H are particle diameter and channel hydraulic diameter, respectively.[9] Figure 1(a) shows particle focusing in a straight rectangular channel and the corresponding forces for both Newtonian and viscoelastic solutions. As can be seen in wall-bounded Poiseuille flow, shear gradient lift force arising from the relative velocity difference around the particle pushes the particles away from the channel center.[43] On the other hand, wall induced lift force originating from the unbalanced pressure distribution over the particles adjacent to the walls repels the particles away from the walls.[44] This pressure dissymmetry caused by fluid flow deceleration between the wall and its adjacent particles increases the pressure in this region and consequently pushes the particles toward the channel center.[45] The Saffman force can be considered zero for a buoyant particle in a Poiseuille flow, since the Stokeslet flow originating from a particle lagging relative to the shear flow is balanced by the Stokeslet velocity field generated by the curvature of the bulk flow.[43] Asmolov derived an equation for the net inertial lift force (F_L) on a rigid sphere in a Poiseuille flow caused by shear gradient and wall induced forces as follows:[46]

$$F_L = C_L \rho_f \gamma^2 a^4, \tag{1}$$

where C_L denotes the dimensionless lift coefficient, γ represents the shear rate, ρ_f is the solution density, and a is the diameter of the particle.

Magnus force originates from the rotation of the sphere particles in an inertial flow and can be described by the following

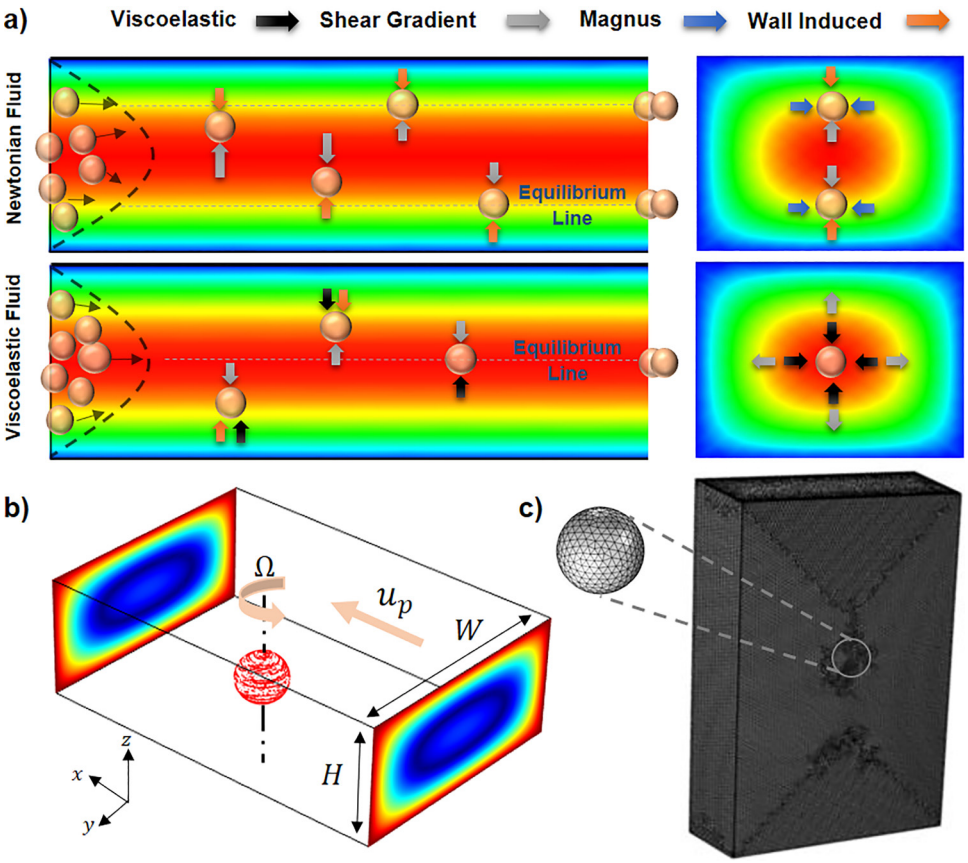

FIG. 1. (a) Different equilibrium positions and their corresponding forces for Newtonian and viscoelastic solutions in a straight rectangular channel. (b) Schematic of the particle modeled in a portion of a rectangular channel for DNS. (c) Mesh configuration for the portion of the channel with a length of 20*a* and boundary mesh on the surface of the particle.

equation:[47]

$$\overrightarrow{F_\Omega} = \frac{1}{8}\pi r a^3 \rho_f (\overrightarrow{u_f} - \overrightarrow{u_p}) \times \vec{\Omega}, \tag{2}$$

where $\vec{\Omega}$ is the vector of angular velocity of the sphere, and u_p and u_f represent the sphere and flow axial velocity, respectively. This force is taken into account in regions where the wall induced and shear gradient lift forces balance each other.

Viscoelastic force arising from the solution viscoelasticity pushes the particles toward the regions with lower shear stress values and can be described as[31]

$$F_E \sim a_p^3 \nabla N_1(\dot{\gamma}), \tag{3}$$

where ∇N_1 and $\dot{\gamma}$ are the gradient of first normal stress difference and average (characteristic) shear rate. For most viscoelastic fluids, $N_2(\dot{\gamma})$ values are very small and can be considered negligible compared to the corresponding $N_1(\dot{\gamma})$ values under most conditions.[48]

B. Direct numerical simulation (DNS) method

In this study, the DNS method was used to precisely model the interactions between flow and particles and to measure the elasto-inertial forces acting on the particles.[49] To this end, flow field through the channel was first calculated using continuity and momentum equations [Eqs. (4) and (5)] by considering the particle as an obstacle only permitted to have free rotational movement [Fig. 1(b)],

$$\nabla \cdot u = 0, \tag{4}$$

$$\rho\left(\frac{\partial u}{\partial t} + (u \cdot \nabla)u\right) = -\nabla p + \eta_s \nabla^2 u + \nabla \cdot \tau. \tag{5}$$

In Eq. (5), τ and η_s are the polymeric part of the extra stress tensor and the Newtonian viscosity of the fluid, respectively.[50] It should be noted that in the case of Newtonian fluid, τ is equal to zero. Yang *et al.*[51] experimentally proved that for low concentration of PEO solution (less than 2500 ppm) the shear-thinning property of the PEO solution can be considered negligible. Since elasticity has more effects on particle migration than the shear-thinning behavior of the PEO solution (2000 ppm),[51,52] Olderoyd B equation [Eq. (6)] was used to calculate the extra stress tensor used in Eq. (5),

$$\tau + \lambda\left(\frac{\delta \tau}{\delta t} + u \cdot \nabla \tau - \nabla u^T \cdot \tau - \tau \cdot \nabla u\right) = \eta_p(\nabla u + \nabla u^T), \tag{6}$$

where λ and η_p indicate the relaxation time and polymeric viscosity, respectively.[50] The value of relaxation time (λ) and viscosity of the PEO solution (η_p) were measured using a capillary breakup

extensional rheometer (CaBER-1, ThermoHakke) and a rotational rheometer (MCR-301, Anton Paar), respectively, which are $\lambda_{mean} = 0.0106$ s and $\eta_p = 0.031$ for PEO solution (2000 ppm).

After solving the momentum equation and obtaining the flow field, particle linear and angular acceleration were obtained based on Newton's second law [Eqs. (7) and (8)] by integrating the total stresses over the particle's surface in all three directions,

$$m\frac{du_p}{dt} = \oint_{\partial V_p} \left[\underbrace{-PI + \eta_s(\nabla u + \nabla u^T)}_{\text{Inertial part}} + \underbrace{\tau}_{\text{Elastic part}} \right] n\, dS, \quad (7)$$

$$I\frac{d\Omega_p}{dt} = \oint_{\partial V_p} r \times \left\{ \left[\underbrace{-PI + \eta_s(\nabla u + \nabla u^T)}_{\text{Inertial part}} + \underbrace{\tau}_{\text{Elastic part}} \right] n \right\} dS. \quad (8)$$

The total stress tensor was divided into two separate inertial and elastic parts [Eqs. (7) and (8)], which enabled us to measure the effects of each force individually. (The whole algorithm for DNS method and lift forces calculation flowchart can be seen in S1 in the supplementary material.) According to Fig. 1(b), a moving wall and slip velocity boundary conditions were used for the channel walls and the particle's surface, respectively. Also, laminar inflow and outflow conditions were considered at the channel inlet and outlet correspondingly. The boundary conditions for the channel and particle with their corresponding values are presented in Table I. In this table, U and $\vec{r}$ indicate the mean inlet velocity and the vector of particle position, respectively. Also, as was shown in Fig. 1(b), $\overrightarrow{u_p}$ and $\vec{\Omega}$ represent the particle axial and angular velocities. Our investigation shows that utilizing 0.5×10^6 elements for the channel and an element size of $0.1a$ on the particle's surface ensures the independency of simulation results with the number of mesh elements [Fig. 1(c)]. The flowchart for the calculation of lift forces applied on a particle located at point (y_1, z_1) is depicted in Fig. S1 in the supplementary material. Initially, the particle was assumed to be at rest, and its angular and axial velocities were set to zero. Utilizing second order upwind scheme, flow field around the particle was solved based on the given boundary conditions (Table I). Then, by means of Eqs. (7) and (8), particle axial and angular velocities were measured to update the boundary conditions. At the next iteration, flow field was solved again with the updated values of the boundary conditions from previous iteration. This iterative solution stops when the absolute values of axial force in X direction ($|F_X|$) and angular momentums in y and z directions ($|M_y|$ and $|M_z|$) become less than a defined threshold. Finally, when the solution converged, lift forces on y-z plane (F_y and F_z) were calculated for further analysis on particle lateral migration. The surface plot of the elasto-inertial lift force can be calculated by repeating the aforementioned steps for all different points of the cross section.

TABLE I. Boundary conditions of the system.

Boundary	Boundary condition	Value
Inlet	Laminar inflow	$U - u_p$
Outlet	Laminar outflow	$U - u_p$
Channel walls	Moving wall	$-u_p$
Particle surface	Slip velocity	$\Omega \times r$

After solving the flow field around particles and measuring the lift forces, the particles' trajectories to their final equilibrium positions needed to be simulated. The momentum equation for a single particle is

$$m_P\vec{\ddot{x}}_P = \vec{F}_{Drag} + \vec{F}_{Inertial\ lift\ force} + \vec{F}_{Elastic\ lift\ force}. \quad (9)$$

Equation (9) was used to predict and measure particle trajectories relative to its original position. The main flow drag force (F_{Drag}) on the particle surface was calculated using the Stokes drag equation[53] as follows:

$$F_{Drag} = 3\pi\mu Ua. \quad (10)$$

In this equation, μ is the solution viscosity and U is the relative velocity. In addition, elastic and inertial lift forces on each cross section can be measured by interpolation of the lift forces obtained at some specific predefined points across that cross section.

III. EXPERIMENTAL SETUP

To investigate the effects of viscoelasticity on particle focusing, 0.1 g polyethylene oxide (PEO, Sigma-Aldrich, $M_w = 2000$ kDa) was dissolved in a 50 ml AutoMACS buffer (Miltenyi Biotec) to make 2000 ppm PEO solution. Then, 3, 5, and 10 μm fluorescent polystyrene particles (Magsphere-Pasadena, CA) were added to the PEO solution to make a final solution with a concentration of 5×10^4 particle/ml. Also, *Saccharomyces cerevisiae* cells (Sigma-Aldrich—yeast from *Saccharomyces cerevisiae*) were added to the PEO solution to make 3×10^6/ml yeast solution. The prepared solutions were loaded into the 10 ml BD plastic syringe and derived through the channels by a Nexus 3000 syringe pump. After assembling the fluidic tubes to the microchannels, they were mounted on the stage of an inverted fluorescence microscope (Nikon Eclipse Ti) for further analysis. To visualize the focusing of yeast cells and fluorescent particles, the bright-field and fluorescence images were captured using high speed (Phantom-VEO 640L) and 14-bit CCD cameras (NIKON DS-Qi1Mc). The microscope objective and the exposure time were set to 10× and 60 μs for bright-field imaging and 10× and 800 ms for fluorescence microscopy. All the analysis and postprocessing on the captured photos have been performed by the free IMAGEJ software.

IV. DEVICE STRUCTURES AND FABRICATION

Four different square, rectangular, trapezoidal, and complex straight channels with the same length and hydraulic diameter of 5 cm and 75 μm were designed to investigate the effect of channel geometry on elasto-inertial focusing. Figure 2 shows the cross-sectional optical micrograph of the channels with their corresponding dimensions.

Microfluidic devices were fabricated via soft lithography on aluminum master mold by pouring a 10:1 degassed mixture of polydimethylsiloxane (PDMS, Sylgard 184, Dow Corning) and curing agent on the molds. Then, after 2 h of curing in an oven at 65 °C, a cured PDMS block was carefully peeled off from the master mold and its inlet and outlet punched through for fluidic access.

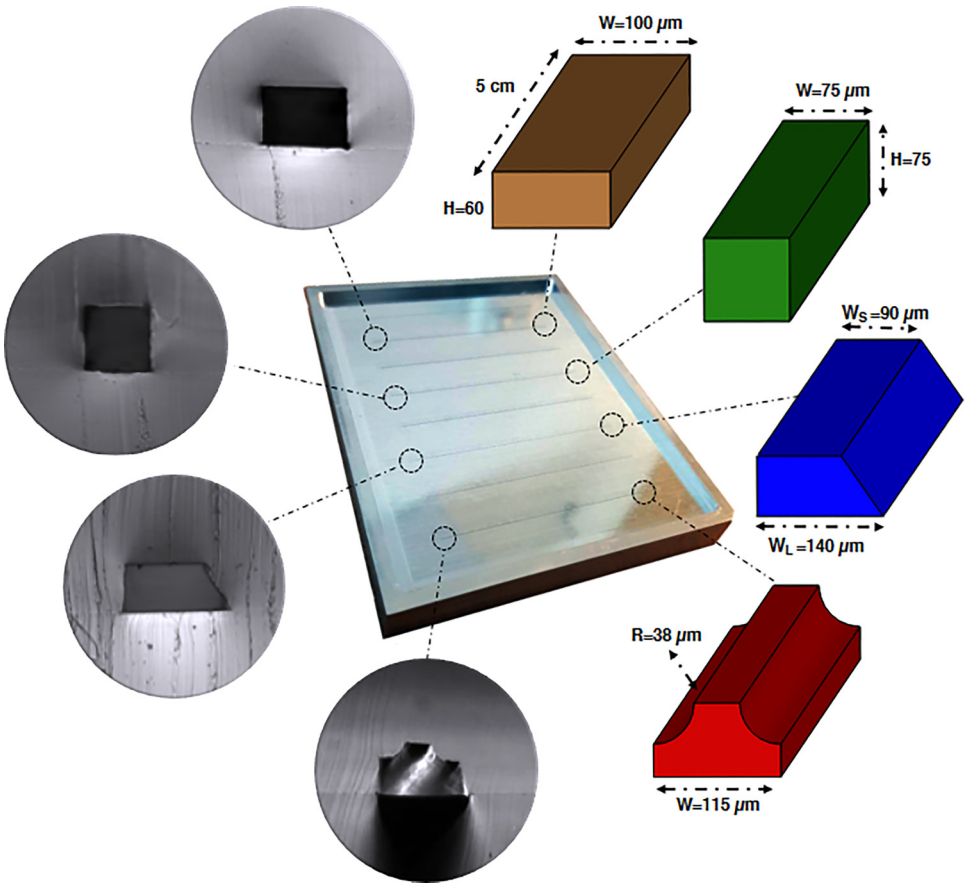

FIG. 2. Schematic of the channels with corresponding dimensions and cross-sectional optical micrograph of the PDMS microfluidic chips.

Finally, the PDMS block was cleaned by 2-propanol to remove the dust and debris and bonded to a cleaned PDMS slab using an oxygen plasma cleaner (Harrick Plasma, PDC-002). It should be noted that the complex channel mold can be easily fabricated by milling a rectangular geometry on an aluminum mold, followed by cutting the upper edges to form the final shape. (Additional information about master mold fabrication and accuracy of the channels can be found in S2 in the supplementary material.)

V. RESULTS AND DISCUSSION

Firstly, elasto-inertial focusing in a straight square channel was investigated to better understand the physics of focusing in viscoelastic fluids. Then, the effect of flow rate, velocity gradient, channel geometry, and corner angles on focusing patterns was comprehensively studied. On the basis of that work, we proposed a new complex channel to obtain a tighter focusing band compared to the other channels under the same hydrodynamic conditions. Finally, we showcased the focusing of 3 μm particles and *Saccharomyces cerevisiae* cells in the complex channel.

A. Physics of elasto-inertial focusing

Figure 3(a) shows the focusing of 10 μm particles in the straight square channel for different flow rates and solutions. As can be seen, for Newtonian solution and flow rates less than 75 μl/min, particles remain scattered within the given channel length as the inertial force is not strong enough to push entire particles toward their equilibrium positions. However, for $Q \geq 100\,\mu$l/min, four distinct focusing bands form due to the strengthening of inertial forces. But for the PEO solution, focusing starts to occur at very low flow rates. It begins with five bands (at corners and the center) at 1 μl/min, followed by one and four focusing bands for flow rates up to 75 μl/min and more than 100 μl/min, respectively. (A video showing the numerical results for focusing of 10 μm particles can be seen in movie 1 of the supplementary material.)

In order to explain these focusing behaviors, we numerically modeled the lateral migration of a dispersed particle in the PEO viscoelastic solution inside the square channel for flow rates of 1 and 25 μl/min [Fig. 3(b)]. It is shown that by increasing the flow rate, by transitioning from a pure elastic to an elasto-inertial regime, the number of focusing bands decreases from five to one. Figures 3(c) and 3(d) show the distribution of inertial and elastic lift forces for a flow rate of 1 μl/min. In central regions (particle a), shear gradient force pushes the particles toward the walls, while elastic force acts in the opposite direction and drives particles to focus at the center. By approaching toward the middle of the side walls (particle b), wall induced and elastic forces become strong

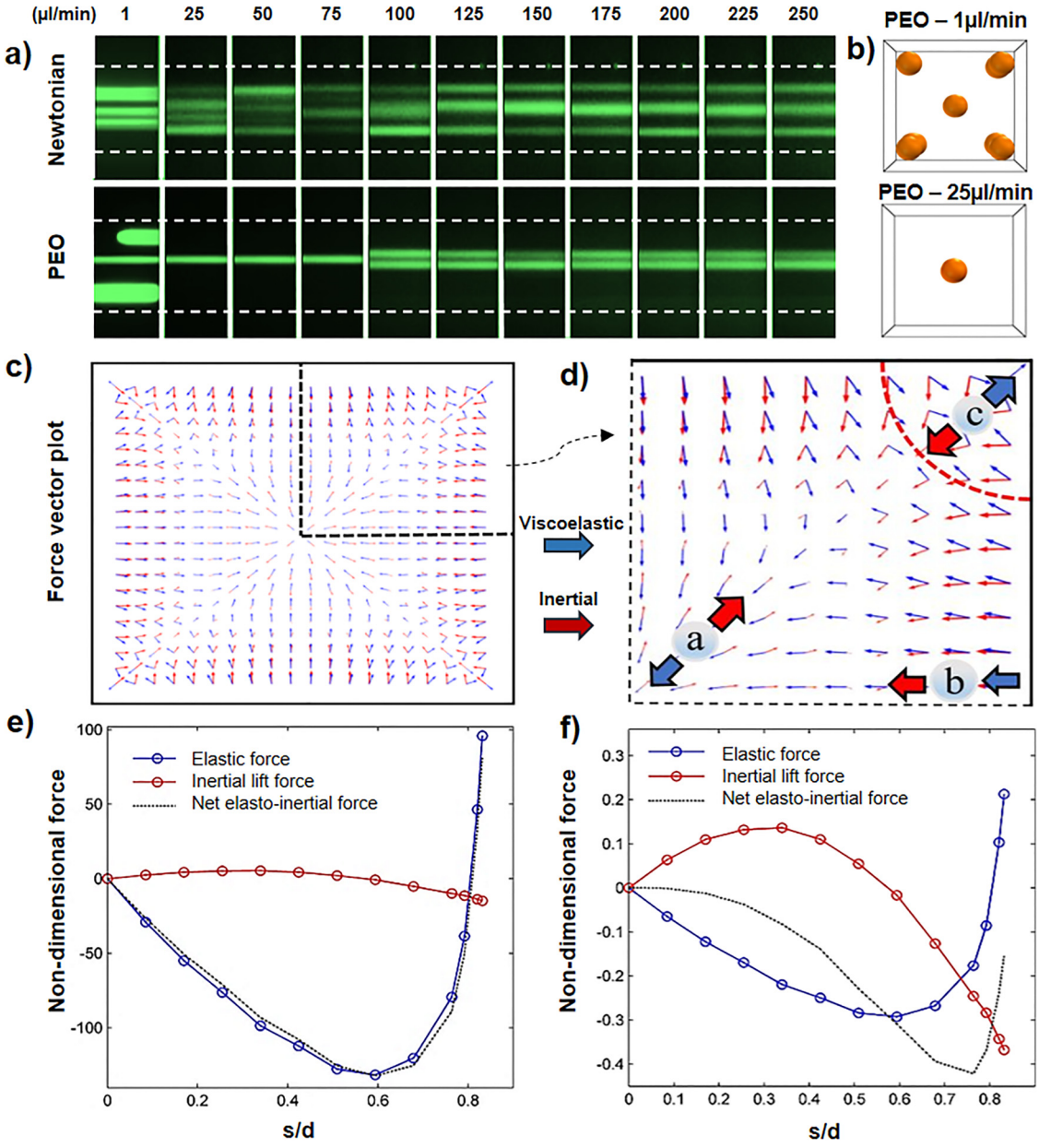

FIG. 3. The mechanism of elasto-inertial focusing in the square channel. (a) Experimental results for focusing positions of 10 μm particles. (b) Numerical results indicating the focusing positions in PEO solution for flow rates of 1 and 25 μl/min. (c) and (d) The inertial and elasticity force vector plot in the cross section of the channel. (e) and (f) Nondimensional applied elasto-inertial forces on the particles for flow rates of 1 and 25 μl/min, respectively.

and unidirectional toward the channel center, which lowers the chance of focusing in these regions. Around the corners (particle c), the elastic force is weak and toward the corner which can be balanced by the opposing inertial lift force. As discussed, equilibrium positions mainly form in the regions where inertial and elastic forces can balance each other [diagonal directions (particles a and c)].

To better describe the competition between inertial and elastic forces to form one and five focusing positions, lift forces are measured along the diagonal direction from the center (s) for flow rates of 1 and 25 μl/min [Figs. 3(e) and 3(f)]. The lift forces were made nondimensional with respect to the term $\rho U_{max}^2 a^4/H^2$ for each of the conditions. In these figures, the positive and negative values denote the

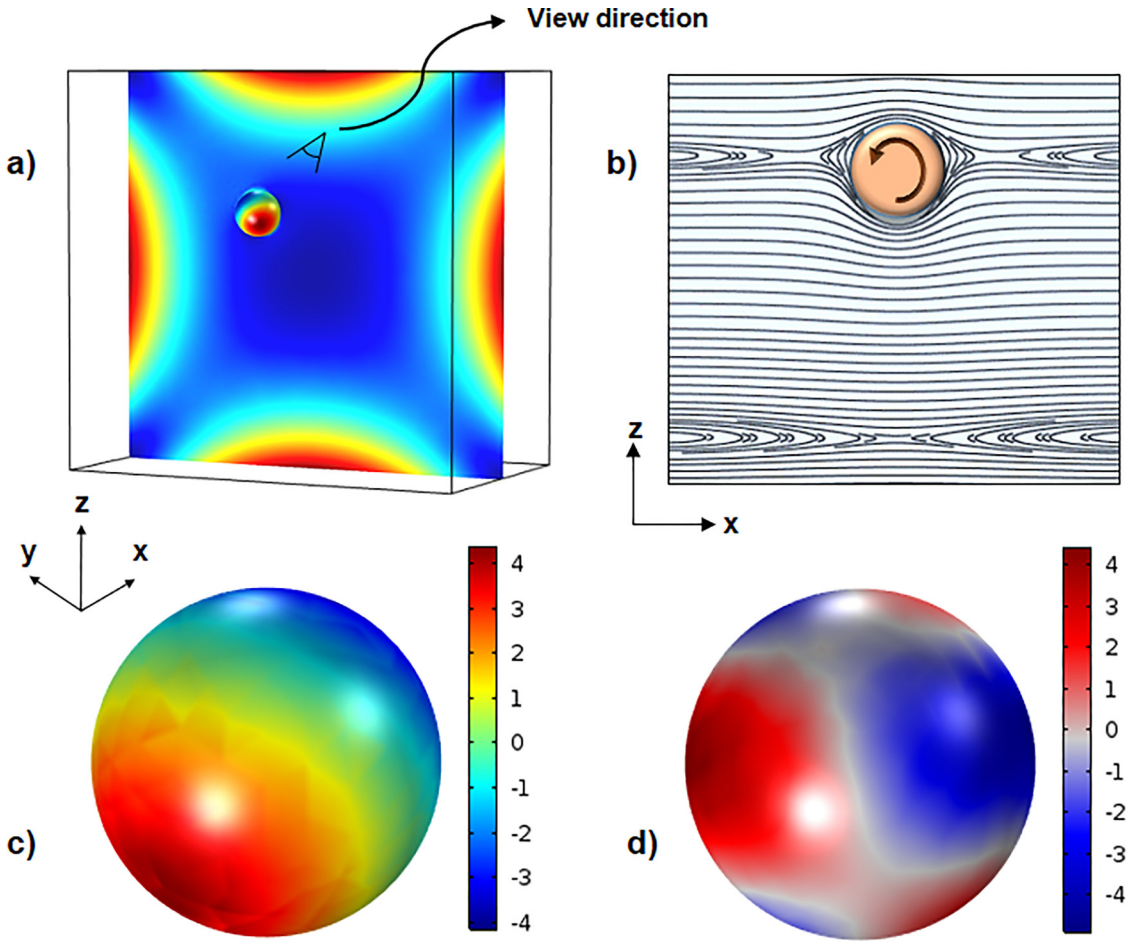

FIG. 4. (a) Contour of first normal stress difference (N_1) and pressure in the cross section of the channel and over the particle, respectively, for a flow rate of 25 μl/min. (b) Streamlines around the particle in the x-z symmetry plane. (c) Distribution of inertial stress on the surface of the particle. (d) Distribution of total elastic stress tensor.

force direction toward the channel center and corner, respectively. As shown in Fig. 3(e), at low flow rates (1 μl/min), the net lift force values are mainly negative (except the regions close to the corners which noticeably increase) with two points equal to zero (at center and s/d $\approx$ 0.8). Therefore, particles in the central region focus at the center, and the rest migrate toward the four focusing positions near the corners. In contrast, by increasing the flow rate to 25 μl/min [Fig. 3(f)], inertial forces become stronger near the corners and repel the particles from the walls. It can be seen that the net elasto-inertial force is negative for all the points on the diagonal resulting particles to focus at the center.

To better understand how elastic and inertial forces act on a particle, first normal stress difference ($N_1 = \tau_{xx} - \tau_{yy}$) is shown inside the channel, and inertial and elastic stresses are depicted on the surface of the particle in Fig. 4. As shown in Fig. 4(a), while N_1 has maximum values near the walls, it has considerably smaller values around the channel center and corners. Streamlines around the particle are depicted in Fig. 4(b). There are three types of streamlines: open stream lines away from the particle, reverse streamlines near the particle changing its direction, and spiraling stream lines which after several rotations around the particle move away due to the presence of the wall near the particle. The distributions of nondimensional inertial and elastic stresses with respect to the 0.5 ρU^2 on the surface of the particle are depicted in Figs. 4(c) and 4(d), respectively. These contours are presented from a view direction shown in Fig. 4(a). As can be seen, the inertial stress is maximum on one side and minimum on the other side, while the elastic stress distribution is more complex with maximum and minimum values at different parts. It can be seen that the highest and lowest values for both inertial and elastic forces are of the same order at the given flow rate (25 μl/min).

B. Particle trajectories in viscoelastic fluid

In this part, particle trajectory through the square channel is presented to illuminate the mechanisms of focusing in viscoelastic

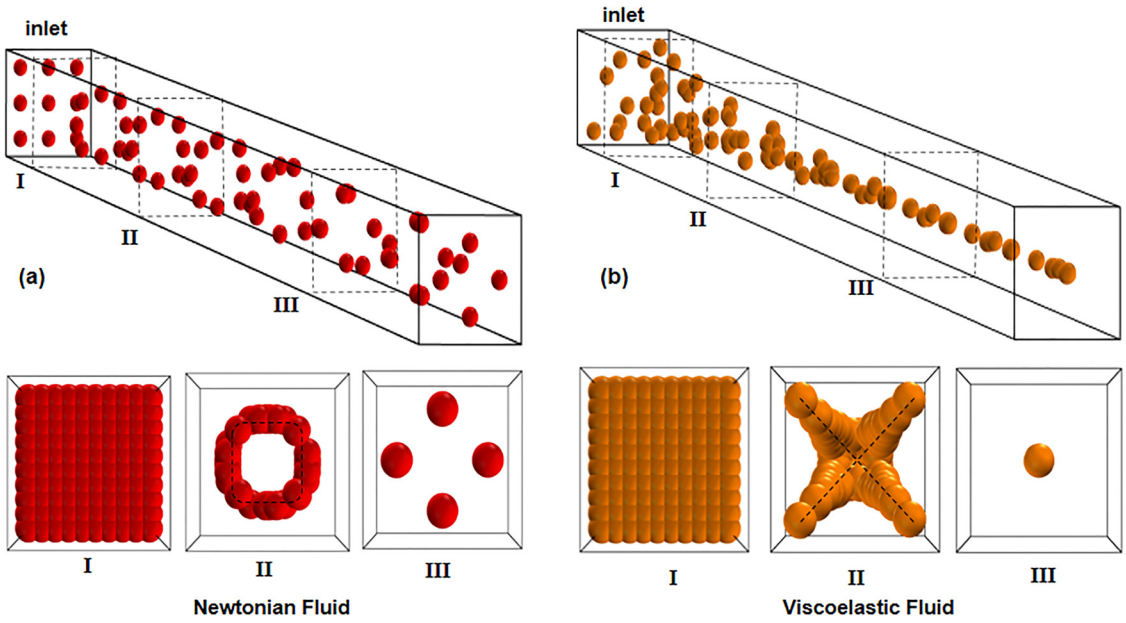

FIG. 5. Particle trajectories of Newtonian (a) and viscoelastic fluid (b) in various cross sections of the straight channel. The black dashed lines in Newtonian fluid are minimum lift force line and in viscoelastic fluid are the minimum shear line.

solutions. According to Fig. 5, the migration of particles to their equilibrium positions can be divided into two stages for both Newtonian and viscoelastic solutions. For Newtonian fluids [Fig. 5(a)], initially particles migrate quickly to the minimum inertial lift regions {curves parallel to the walls [Fig. 5(aII)]} due to the strong shear gradient and wall induced lift forces at the core region and near the walls, respectively. Then, Magnus force pushes the particles slowly toward their final equilibrium positions [Fig. 5(aIII)]. However, in viscoelastic fluids [Fig. 5(b)], particles first move toward the minimum elastic lift regions {diagonal directions [Fig. 5(bII)]} and afterward migrate diagonally toward the minimum shear gradient points [Fig. 5(bIII)]. (The two-stage focusing model can be seen in movie 2 of the supplementary material.)

C. Effect of velocity gradient on focusing pattern

Detailed investigation of the velocity gradient as one of the practical tools in particle sorting is of a great importance. As inertial forces are strongly correlated to the shear rate ($F_L \propto \gamma^2$), changes in flow rate and velocity gradient can noticeably alter the focusing positions. It should be noted that the flow rate increase in wall-bounded Poiseuille flow increases the velocity gradient and subsequently strengthens the inertial forces. Figure 6(a) shows the focusing patterns of 10 μm size particles through the rectangular channel with an aspect ratio of 1.6 for different flow rates. At low flow rates (25 μl/min), particles only focus at the channel center, but increasing the flow rate to 50 μl/min causes focusing to occur in two bands. The side view shows a single line focusing for all the given flow rates, so lift forces were investigated on the horizontal symmetry plane along the Y axis [Fig. 1(b)] to elucidate the transition from one to two line focusing. As previously mentioned, inertial and elastic lift forces oppose each other near the center of the channel and the interaction between these two forces defines the final focusing positions. Figures 6(b) and 6(c) demonstrate the non-dimensional lift forces along the Y direction in the symmetry plane for flow rates of 25 and 50 μl/min. In these figures, negative values of elastic force are presented to better compare the magnitude of elastic and inertial forces. Due to symmetry, the forces are only studied in the first quarter of rectangular cross section. For flow rate of 25 μl/min [Fig. 6(b)], elastic force is stronger than inertial force everywhere which causes all the particles to focus at the center. However, for 50 μl/min flow rate [Fig. 6(c)], there are two regions near the center (separated by the dashed black line), in which elastic and inertial forces are dominant. Although inertial force is dominant between the center of the channel and y/h = 0.42 (h = H/2), elastic force is stronger on the other side of the dashed line from y/h = 0.42 to the wall. As a result, while particles in central region are pushed toward the walls, at around y/h = 0.42, elastic force becomes stronger and pushes the particles in the opposite direction, causing them to reach equilibrium at y/h = 0.42 (about 12.5 μm) distance from the center. (The two line focusing model for viscoelastic solution can be seen in movie 3 of the supplementary material.)

D. Effect of geometry on focusing

In inertial microfluidic systems, channel geometry has proven to play a pivotal role in controlling particle movements due to the strong correlation between inertial forces and the characteristic

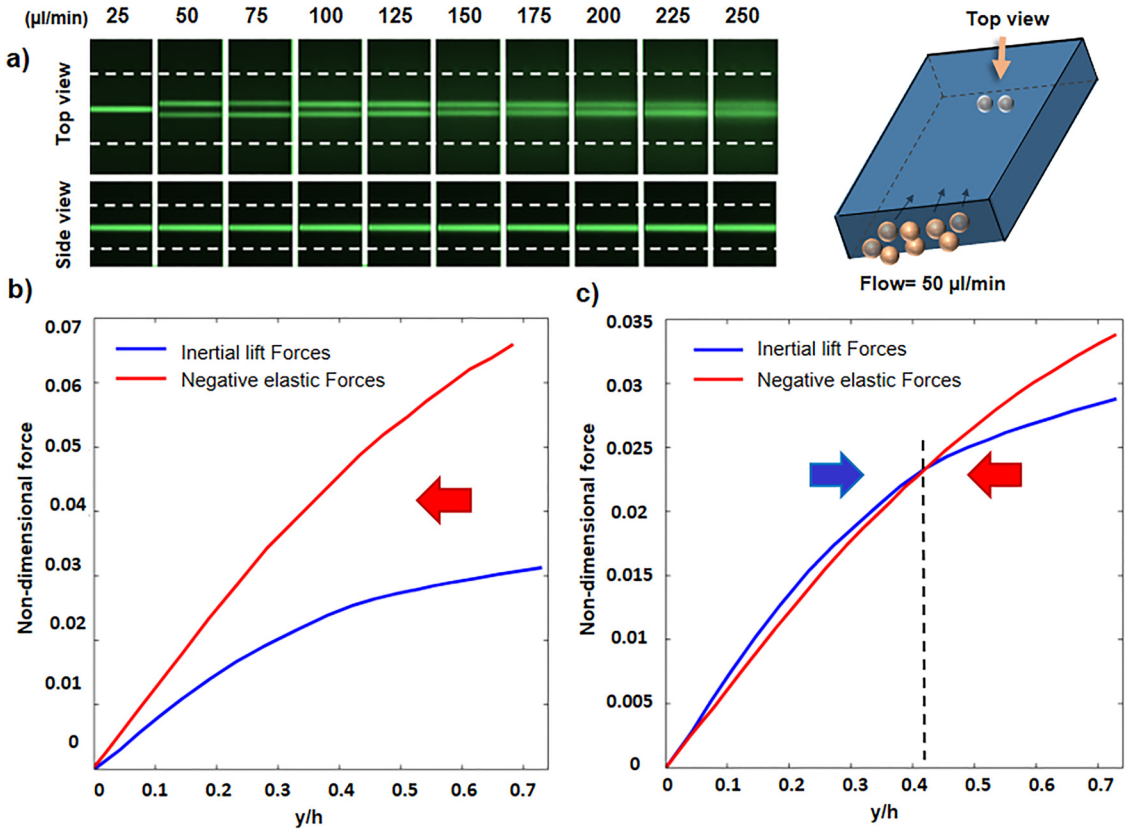

FIG. 6. Elasto-inertial focusing in the rectangular channel. (a) Top and side views of equilibrium positions for a rectangular channel with an aspect ratio of 1.6. (b) and (c) Nondimensional inertial lift force and negative value of nondimensional elastic force near the center of the channel for two different flow rates of 25 ml/min (b) and 50 ml/min (c). Curve intersections are the equilibrium positions.

length of the channel. While many efforts have been performed to increase the efficiency of these systems by employing trapezoidal, semicircular, and triangular channels,[54,55] no one has previously explored the effects of shape nonorthogonality and corner angles on particle sorting. In this section, to evaluate how geometry can affect the focusing behaviors, first the impacts of aspect ratio on the lift forces are explained. Afterward, elastic force along the bisector of various corner angles is evaluated to determine the effects of corner angle on viscoelastic forces. Finally, based on the results of these investigations, a new complex channel is proposed to obtain tighter focusing bands than can be achieved with conventional straight channels.

Figure 7(a) shows focusing of 10 μm particles in trapezoidal, square, and rectangular straight channels with the same hydraulic diameter. It can be clearly seen that for flow rates of 50 and 75 μl/min, the square channel has one focusing band, while the rectangular channel has two. To explain this focusing behavior, we note the correlation between inertial and elastic forces with the width of the channel along the Y axis. Toward the center of the channel, the inertial and elastic forces scale as $F_L \propto \rho_f U_m^2 a^3 / W$[26] and $F_e \propto a^3 \eta_p \lambda \nabla \dot{\gamma}^2 \propto a^3 \eta_p \lambda U_m^2 / W^3$,[56] respectively. Also, the core fluid in the square channel is more confined to the walls than in the rectangular channel of which one side is noticeably longer than the other side. Therefore, by increasing the width of the cross section (W) the elastic force decreases more rapidly than the inertial force, which induces the focusing position to increase to two bands in the rectangular channel at lower flow rates.

Since the elastic force is closely proportional to normal stress difference (∇N_1), Fig. 7(b) shows the ∇N_1 contours in trapezoidal, square, and rectangular channels instead of elastic force. As can be seen, increasing the angle of the corner results in stronger elastic force around it. According to Fig. 7(a), in the trapezoidal channel, for flow rates of 75–150 μl/min, the focusing band in the proximity of the "50° corner" slightly shifts toward this corner, proving that the elastic force in this region is weaker than the other corners. To better describe the effects of corner angle on viscoelastic force, ∇N_1 values are measured along the line connecting the center to corners A and B [shown in Fig. 7(b)] and the radial direction in a circular channel. All the channels assumed to have the same hydraulic diameter of 75 μm and flow rate of 25 μl/min to equalize the hemodynamic conditions. According to Fig. 7(c), increasing the angle of the corner has two significant effects on

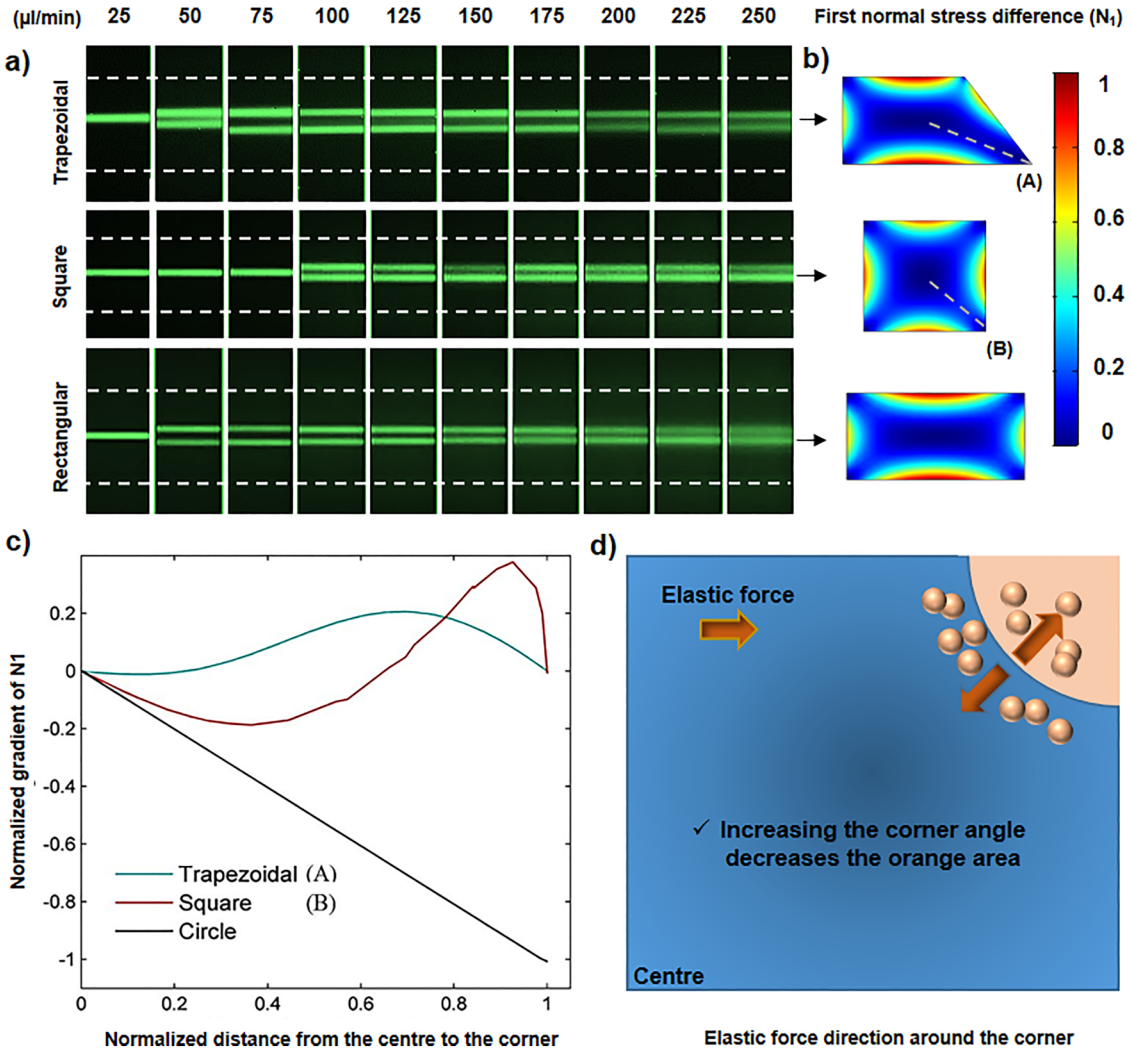

FIG. 7. (a) Top views of the particle trajectories in trapezoidal, square, and rectangular channels. The transition from one to two focusing bands occurs at higher flow rate in the square channel under the same conditions. (b) First normal stress difference contours in the corresponding channels. (c) Effects of corner angle on normalized gradient of N_1 as an indicator of elastic force. Corners A and B have angles of 50° and 90°, respectively. A circular channel is assumed to have the corner angle of 180°. (d) Direction of elastic force in the first quarter of square cross section. The direction of elastic force in the blue region is always toward the center while in the orange region is in the opposite direction.

∇N_1. First, the regions in which ∇N_1 has negative values increase, which means elastic force can drive the particles toward the center more effectively. Second, the value of elastic force rises, indicating this force becomes stronger.

As shown for the circular channel with an angle of 180°, since the value of ∇N_1 is negative everywhere, the elastic force pushes the particles toward the center from all the regions. However, for trapezoidal and square geometries, there are some regions around the corners where the elastic force acts in the opposite direction and inhibits the tight single-band focusing at the center. Figure 7(d) shows one of these regions (orang quadrant) around the corner of the square channel. Since increasing the corner's area can increase the elastic force and changes its direction toward the center (as for a circular channel), it might be possible by some modification in the rectangular geometry (as the most common cross section used in inertial microfluidic systems) to obtain tighter focusing for wider range of Reynolds number and concentrate smaller microparticles more accurately.

As a summary of Secs. V A–V D, we concluded that in order to improve focusing, the following points should be considered:

1. The corner angle of the cross sections should be as large as possible. This encourages particle migration toward the center of the channel.

2. At the same hydraulic diameter, the core flow needs to be as confined as possible in all directions. This causes particles to remain focused at the center for higher flow rates.

E. Designing the complex channel

In this section, based on our understanding about the mechanisms of elasto-inertial focusing, we proposed a new complex straight channel to obtain tighter particle focusing band for smaller microparticles and wider range of flow rates. According to Fig. 7(d), this geometry is designed by cutting the upper corners of the rectangular channel (as shown in Fig. 2) and resizing the sides to have the same hydraulic diameter as other channels. This geometry modification promotes focusing by two mechanisms. Firstly, compared to the rectangular channel, wider corners in the complex channel shrink the regions where elastic force is directed toward the corners. In addition, it causes the elastic force to become more dominant in the core region and improves the focusing there. Secondly, due to its nonlinear shape, the core flow around the center of the channel is more confined and has more similar values in both vertical and horizontal directions, causing the channel to have tighter focusing at higher flow rates. Figure 8(a) shows the elasto-inertial focusing positions of 5 μm particles through the square, rectangular, and complex channels for a wide range of flow rates. It can be seen that, in contrast to square and rectangular channels, the complex channel has single-band focusing at flows up to 100 μl/min. In addition, as shown by intensity profile in Fig. 8(c), the complex channel has tighter focusing compared to the rectangular and square

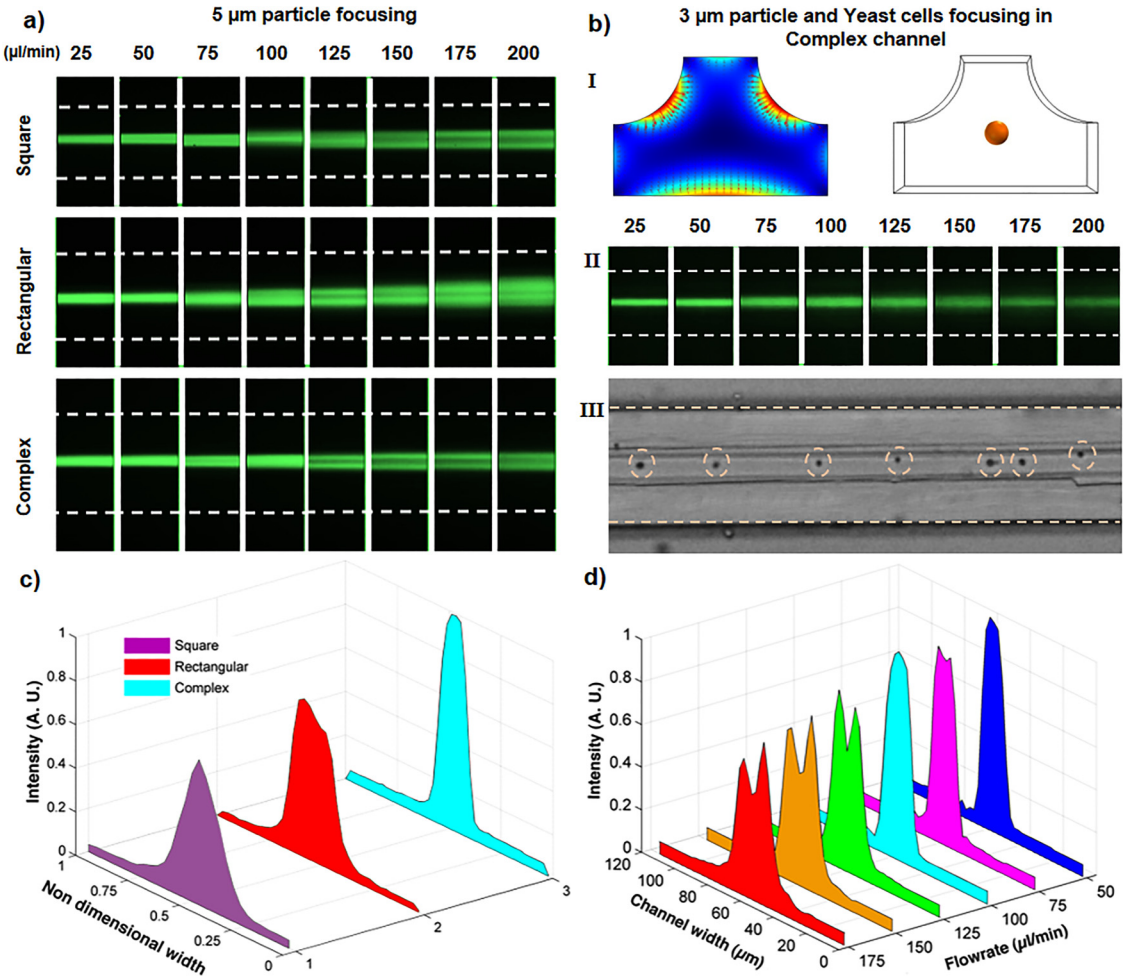

FIG. 8. Focusing positions in square, rectangular, and complex channels. (a) Top view focusing positions of 5 μm particles, which shows for all the flow rates the complex channel has tighter focusing compared to the conventional channels. (bI) Elasto-inertial force vector plot in the modified complex channel and the focusing position for 3 μm particles. (bII) Top view focusing of the 3 μm fluorescent particles in the modified complex channel. (bIII) Focusing of the yeast cells in the complex channel for a flow rate of 75 μl/min. (c) Intensity profiles for the focusing of 5 μm particles at a flow rate of 100 μl/min, which shows a tighter focusing in the complex channel. (d) Intensity profiles for focusing of 5 μm particles through the complex channel.

channels at 100 μl/min flow rate. For flow rates greater than 100 μl/min, although the focusing band splits in the complex channel, it still shows an enhanced focusing in the central region [Fig. 8(d)]. It should be noted that while the complex channel has longer width compare to its counterpart geometries, interestingly it has tighter focusing, which makes this channel a better option for flow cytometry and particle separation applications. Figure 8(b) represents the viscoelastic and inertial lift forces in a cross section of the complex channel. According to the N_1 contours shown in Fig. 8(bI), elastic forces are stronger in the complex channel and are more unidirectional toward the channel center, compared to the other channels. After verifying the tighter focusing in the complex channel, we modified its dimensions (W = 100, H = 30, and R = 38) to focus 3 μm particles [Fig. 8(bII)]. Interestingly, the 3 μm particles remain focused up to a flow rate of 100 μl/min. Finally, as a proof of concept, we showcased the focusing of *Saccharomyces cerevisiae* cells (3–5 μm) with a flow rate of 75 μl/min [Fig. 8(bIII)]. Dashed circles show the position of yeast cells at the central region of the channel. (A video showing the focusing of the 3 μm particles and yeast cells in the complex channel can be seen in movie 4 of the supplementary material.)

VI. CONCLUSION

In this work, we experimentally and numerically studied the elasto-inertial focusing in different straight channels to investigate the effects of cross-sectional geometry accompanied with viscoelasticity on the focusing phenomenon. We presented a two-stage elasto-inertial focusing model within straight channels, in which particles first move toward the lowest elastic force regions (diagonal directions in rectangular and square channels) and then diagonally migrate to their final equilibrium positions. Furthermore, for the first time, we explored the effects of corner angle on the viscoelastic force. The results revealed that increasing the angle of the corner not only strengthens the elastic forces, but also directs them more toward the channel center, even in areas near the corners. Also, the core flow needs to be as confined as possible in all directions to have the best focusing at the center. We then studied the effects of velocity gradient and aspect ratio on the focusing positions. We found that increasing the channel width weakens the elastic force more than the inertial force, causing one focusing band in a square channel to increase to two bands in a rectangular channel. Based on our findings, we developed a novel complex channel design to obtain a tighter focusing under the same conditions. We were able to use elasto-inertial forces to focus 3 μm particles in the complex channel at a high flow rate of 100 μl/min. Finally, as a proof of concept, we showcased the elasto-inertial focusing of the *Saccharomyces cerevisiae* cells (3–5 μm) with a high throughput of 75 μl/min. We are of the opinion that our findings will provide a deeper understanding of the fundamentals of elasto-inertial focusing and will serve as a strong basis for further design of complex channels.

SUPPLEMENTARY MATERIAL

In the supplementary material, supplementary one (S1) gives extra information about the flowchart and steps used for the calculation of lift forces. Supplementary two (S2) provides information about fabrication process and the accuracy of the master molds. Supplementary movie 1 shows the numerical results for the focusing of 10 μm particles in the square channel for Newtonian and viscoelastic solutions. Supplementary movie 2 shows the modeling of two-stage focusing in the straight square channel for both Newtonian and viscoelastic solutions. Supplementary movie 3 shows the simulation results for the elasto-inertial focusing of 10 μm particles in a rectangular channel for a flow rate of 50 μl/min. Supplementary movie 4 shows the focusing of 3 μm particles and yeast cells at the center of the complex channel numerically and experimentally (the concentration of the yeast cells is 3×10^6 per ml).

ACKNOWLEDGMENTS

This research work is supported by the National Health and Medical Research Council via the career development fellowship (No. APP1143377) and the Australian Research Council through discovery project grants (Nos. DP170103704 and DP180103003).

REFERENCES

[1]J. Zhang *et al.*, "Fundamentals and applications of inertial microfluidics: A review," Lab Chip **16**(1), 10–34 (2016).
[2]T. P. Forbes and S. P. Forry, "Microfluidic magnetophoretic separations of immunomagnetically labeled rare mammalian cells," Lab Chip **12**(8), 1471–1479 (2012).
[3]Z. Wang and J. Zhe, "Recent advances in particle and droplet manipulation for lab-on-a-chip devices based on surface acoustic waves," Lab Chip **11**(7), 1280–1285 (2011).
[4]B. Çetin and D. Li, "Dielectrophoresis in microfluidics technology," Electrophoresis **32**(18), 2410–2427 (2011).
[5]S. R. Bazaz *et al.*, "A hybrid micromixer with planar mixing units," RSC Adv. **8** (58), 33103–33120 (2018).
[6]D. Di Carlo, "Inertial microfluidics," Lab Chip **9**(21), 3038–3046 (2009).
[7]M. Yamada, M. Nakashima, and M. Seki, "Pinched flow fractionation: Continuous size separation of particles utilizing a laminar flow profile in a pinched microchannel," Anal. Chem. **76**(18), 5465–5471 (2004).
[8]G. Segre and A. Silberberg, "Radial particle displacements in Poiseuille flow of suspensions," Nature **189**(4760), 209 (1961).
[9]D. Di Carlo *et al.*, "Continuous inertial focusing, ordering, and separation of particles in microchannels," Proc. Natl. Acad. Sci. **104**(48), 18892–18897 (2007).
[10]S. C. Hur, A. J. Mach, and D. Di Carlo, "High-throughput size-based rare cell enrichment using microscale vortices," Biomicrofluidics **5**(2), 022206 (2011).
[11]H. Ryu *et al.*, "Patient-derived airway secretion dissociation technique to isolate and concentrate immune cells using closed-loop inertial microfluidics," Anal. Chem. **89**(10), 5549–5556 (2017).
[12]M. E. Warkiani *et al.*, "Ultra-fast, label-free isolation of circulating tumor cells from blood using spiral microfluidics," Nat. Protoc. **11**(1), 134 (2016).
[13]H. W. Hou *et al.*, "Isolation and retrieval of circulating tumor cells using centrifugal forces," Sci. Rep. **3**, 1259 (2013).
[14]B. R. Mutlu *et al.*, "Non-equilibrium inertial separation array for high-throughput, large-volume blood fractionation," Sci. Rep. **7**(1), 9915 (2017).
[15]J. Zhang *et al.*, "High-throughput separation of white blood cells from whole blood using inertial microfluidics," IEEE T Biomed. Circ. Syst. **11**(6), 1422–1430 (2017).
[16]M. Antfolk and T. Laurell, "Continuous flow microfluidic separation and processing of rare cells and bioparticles found in blood—A review," Anal. Chim. Acta **965**, 9–35 (2017).
[17]M. S. Syed *et al.*, "Selective separation of microalgae cells using inertial microfluidics," Bioresour. Technol. **252**, 91–99 (2018).
[18]X. Wang *et al.*, "A low-cost, plug-and-play inertial microfluidic helical capillary device for high-throughput flow cytometry," Biomicrofluidics **11**(1), 014107 (2017).

[19]K. T. Kotz *et al.*, "System and method for inertial focusing cytometer with integrated optics for particle characterization," U.S. patent 10,139,333 B2 (27 November, 2018).
[20]R. Moloudi *et al.*, "Inertial particle focusing dynamics in a trapezoidal straight microchannel: Application to particle filtration," Microfluid. Nanofluid. **22**(3), 33 (2018).
[21]Q. Zhao *et al.*, "Flow rate-insensitive microparticle separation and filtration using a microchannel with arc-shaped groove arrays," Microfluid. Nanofluid. **21** (3), 55 (2017).
[22]M. E. Warkiani *et al.*, "Membrane-less microfiltration using inertial microfluidics," Sci. Rep. **5**, 11018 (2015).
[23]J. Zhang *et al.*, "Inertial focusing in a straight channel with asymmetrical expansion–contraction cavity arrays using two secondary flows," J. Micromech. Microeng. **23**(8), 085023 (2013).
[24]J. Zhang *et al.*, "Particle inertial focusing and its mechanism in a serpentine microchannel," Microfluid. Nanofluid. **17**(2), 305–316 (2014).
[25]B. R. Mutlu, J. F. Edd, and M. Toner, "Oscillatory inertial focusing in infinite microchannels," Proc. Nat. Acad. Sci. U.S.A. **115**(30), 7682–7687 (2018).
[26]D. Di Carlo *et al.*, "Particle segregation and dynamics in confined flows," Phys. Rev. Lett. **102**, 094503 (2009).
[27]A. T. Ciftlik, M. Ettori, and M. A. Gijs, "High throughput-per-footprint inertial focusing," Small **9**(16), 2764–2773 (2013).
[28]M. A. Faridi *et al.*, "Elasto-inertial microfluidics for bacteria separation from whole blood for sepsis diagnostics," J. Nanobiotechnol. **15**(1), 3 (2017).
[29]D. Yuan *et al.*, "Dean-flow-coupled elasto-inertial three-dimensional particle focusing under viscoelastic flow in a straight channel with asymmetrical expansion–contraction cavity arrays," Biomicrofluidics **9**(4), 044108 (2015).
[30]A. Karnis and S. Mason, "Particle motions in sheared suspensions. XIX. Viscoelastic media," Trans. Soc. Rheol. **10**(2), 571–592 (1966).
[31]N. Xiang *et al.*, "Fundamentals of elasto-inertial particle focusing in curved microfluidic channels," Lab Chip **16**(14), 2626–2635 (2016).
[32]S. Yang *et al.*, "Deformability-selective particle entrainment and separation in a rectangular microchannel using medium viscoelasticity," Soft Matter **8**(18), 5011–5019 (2012).
[33]K. W. Seo *et al.*, "Particle migration and single-line particle focusing in microscale pipe flow of viscoelastic fluids," RSC Adv. **4**(7), 3512–3520 (2014).
[34]S. Cha *et al.*, "Cell stretching measurement utilizing viscoelastic particle focusing," Anal. Chem. **84**(23), 10471–10477 (2012).
[35]J. Nam *et al.*, "Continuous separation of microparticles in a microfluidic channel via the elasto-inertial effect of non-Newtonian fluid," Lab Chip **12**(7), 1347–1354 (2012).
[36]C. Liu *et al.*, "Size-based separation of particles and cells utilizing viscoelastic effects in straight microchannels," Anal. Chem. **87**(12), 6041–6048 (2015).
[37]C. Liu *et al.*, "Field-free isolation of exosomes from extracellular vesicles by microfluidic viscoelastic flows," ACS Nano **11**(7), 6968–6976 (2017).
[38]J. Nam *et al.*, "Microfluidic device for sheathless particle focusing and separation using a viscoelastic fluid," J. Chromatogr. A **1406**, 244–250 (2015).
[39]S. Yang *et al.*, "Sheathless elasto-inertial particle focusing and continuous separation in a straight rectangular microchannel," Lab Chip **11**(2), 266–273 (2011).
[40]D. Yuan *et al.*, "Sheathless Dean-flow-coupled elasto-inertial particle focusing and separation in viscoelastic fluid," RSC Adv. **7**(6), 3461–3469 (2017).
[41]G. Li, G. H. McKinley, and A. M. Ardekani, "Dynamics of particle migration in channel flow of viscoelastic fluids," J. Fluid Mech. **785**, 486–505 (2015).
[42]N. Patankar *et al.*, "Lift-off of a single particle in Newtonian and viscoelastic fluids by direct numerical simulation," J. Fluid Mech. **438**, 67–100 (2001).
[43]J. Matas, J. Morris, and E. Guazzelli, "Lateral forces on a sphere," Oil Gas Sci. Technol. **59**(1), 59–70 (2004).
[44]R. Cox and S. Hsu, "The lateral migration of solid particles in a laminar flow near a plane," Int. J. Multiphase Flow **3**(3), 201–222 (1977).
[45]J. M. Martel and M. Toner, "Inertial focusing in microfluidics," Annu. Rev. Biomed. Eng. **16**, 371–396 (2014).
[46]E. S. Asmolov, "The inertial lift on a spherical particle in a plane Poiseuille flow at large channel Reynolds number," J. Fluid Mech. **381**, 63–87 (1999).
[47]S. Rubinow and J. B. Keller, "The transverse force on a spinning sphere moving in a viscous fluid," J. Fluid Mech. **11**(3), 447–459 (1961).
[48]H. Lim, J. Nam, and S. Shin, "Lateral migration of particles suspended in viscoelastic fluids in a microchannel flow," Microfluid. Nanofluid. **17**(4), 683 (2014).
[49]A. Shamloo and A. Mashhadian, "Inertial particle focusing in serpentine channels on a centrifugal platform," Phys. Fluids **30**(1), 012002 (2018).
[50]H. Giesekus, "A simple constitutive equation for polymer fluids based on the concept of deformation-dependent tensorial mobility," J. Nonnewton. Fluid Mech. **11**(1), 69–109 (1982).
[51]S. H. Yang *et al.*, "Multiple-line particle focusing under viscoelastic flow in a microfluidic device," Anal. Chem. **89**(6), 3639–3647 (2017).
[52]D. Li and X. Xuan, "Fluid rheological effects on particle migration in a straight rectangular microchannel," Microfluid. Nanofluid. **22**(4), 49 (2018).
[53]J. F. Richardson and J. H. Harker, *Chemical Engineering—Volume 2 Particle Technology and Separation Processes* (Butterworth-Heinemann, 2002).
[54]M. E. Warkiani *et al.*, "Slanted spiral microfluidics for the ultra-fast, label-free isolation of circulating tumor cells," Lab Chip **14**(1), 128–137 (2014).
[55]J.-A. Kim *et al.*, "Inertial focusing in non-rectangular cross-section microchannels and manipulation of accessible focusing positions," Lab Chip **16**(6), 992–1001 (2016).
[56]H. Amini, W. Lee, and D. Di Carlo, "Inertial microfluidic physics," Lab Chip **14**(15), 2739–2761 (2014).